

Thermoelectric properties of In-rich InGaN and InN/InGaN superlattices

Cite as: AIP Advances 6, 045216 (2016); <https://doi.org/10.1063/1.4948446>

Submitted: 23 October 2015 • Accepted: 18 April 2016 • Published Online: 28 April 2016

James (Zi-Jian) Ju,  Bo Sun, Georg Haunschild, et al.



View Online



Export Citation



CrossMark

ARTICLES YOU MAY BE INTERESTED IN

[The structural properties of InGaN alloys and the interdependence on the thermoelectric behavior](#)


AIP Advances 6, 025305 (2016); <https://doi.org/10.1063/1.4941934>

[High temperature thermoelectric properties of optimized InGaN](#)

Journal of Applied Physics 110, 123709 (2011); <https://doi.org/10.1063/1.3670966>

[Calculated thermoelectric properties of \$\text{In}_x\text{Ga}_{1-x}\text{N}\$, \$\text{In}_x\text{Al}_{1-x}\text{N}\$, and \$\text{Al}_x\text{Ga}_{1-x}\text{N}\$](#)

Journal of Applied Physics 113, 183707 (2013); <https://doi.org/10.1063/1.4804174>



Thermoelectric properties of In-rich InGaN and InN/InGaN superlattices

James (Zi-Jian) Ju,¹ Bo Sun,² Georg Haunschild,¹ Bernhard Loitsch,¹ Benedikt Stoib,¹ Martin S. Brandt,¹ Martin Stutzmann,¹ Yee Kan Koh,² and Gregor Koblmüller^{1,a}

¹Walter Schottky Institut, Physik Department, TU München, 85748 Garching, Germany

²Department of Mechanical Engineering, National University of Singapore, 117576, Singapore

(Received 23 October 2015; accepted 18 April 2016; published online 28 April 2016)

The thermoelectric properties of n-type InGaN alloys with high In-content and InN/InGaN thin film superlattices (SL) grown by molecular beam epitaxy are investigated. Room-temperature measurements of the thermoelectric properties reveal that an increasing Ga-content in ternary InGaN alloys ($0 < x(\text{Ga}) < 0.2$) yields a more than 10-fold reduction in thermal conductivity (κ) without deteriorating electrical conductivity (σ), while the Seebeck coefficient (S) increases slightly due to a widening band gap compared to binary InN. Employing InN/InGaN SLs ($x(\text{Ga}) = 0.1$) with different periods, we demonstrate that confinement effects strongly enhance electron mobility with values as high as $\sim 820 \text{ cm}^2/\text{Vs}$ at an electron density n_e of $\sim 5 \times 10^{19} \text{ cm}^{-3}$, leading to an exceptionally high σ of $\sim 5400 (\Omega\text{cm})^{-1}$. Simultaneously, in very short-period SL structures S becomes decoupled from n_e , κ is further reduced below the alloy limit ($\kappa < 9 \text{ W/m-K}$), and the power factor increases to $2.5 \times 10^{-4} \text{ W/m-K}^2$ by more than a factor of 5 as compared to In-rich InGaN alloys. These findings demonstrate that quantum confinement in group-III nitride-based superlattices facilitates improvements of thermoelectric properties over bulk-like ternary nitride alloys. © 2016 Author(s). All article content, except where otherwise noted, is licensed under a Creative Commons Attribution (CC BY) license (<http://creativecommons.org/licenses/by/4.0/>). [<http://dx.doi.org/10.1063/1.4948446>]

I. INTRODUCTION

The family of group-III nitride semiconductors is nowadays one of the key players in commercial solid-state lighting and high-power/high-frequency electronics.^{1,2} These versatile materials are increasingly also explored as potential candidates for solid-state thermoelectric energy conversion technologies.^{3–5} This is motivated mainly by the increased desire for on-chip power generation and on-spot thermal management of excess heat in complex nitride-based optoelectronic and electronic devices with ever shrinking device dimensions.⁵ Such monolithically integrated platforms, capable of adding thermoelectric device functionality, are highly attractive in group-III nitrides particularly because of the widely available infrastructure of GaN-based technology.

The performance of thermoelectric materials is largely determined by their viability as robust materials in harsh and caustic conversion environments, and the well-known interplay of three characteristic parameters, i.e., the Seebeck coefficient S , the electrical conductivity σ , and the thermal conductivity κ , via the temperature-dependent figure of merit defined as $ZT(T) = S^2\sigma T/\kappa$. Inherently, the non-toxic group-III nitrides offer outstanding thermal and mechanical stability, excellent radiation hardness, as well as widely tunable band gaps and excellent control over electrical conductivity needed for tuning thermoelectric properties. So far, the thermoelectric properties of a wide range of binary and ternary nitride alloys have been investigated, e.g. GaN [Refs. 5–8] and InN [Refs. 4, 9, and 10] binaries, as well as of ternary AlGaIn [Refs. 3 and 7], InGaIn [Refs. 11–13]

^aCorresponding Author: Gregor.KoblmueLLer@wsi.tum.de

and InAlN [Refs. 3, 4, and 14–16] alloys. Clearly, while the thermoelectric prospects for binary group-III-nitrides are rather poor due to their very high thermal conductivities (> 90 W/m-K),¹⁷ ternary nitride alloys exhibit much improved thermoelectric properties^{10–15} since alloying significantly reduces thermal conductivity.^{18,19} Further progress has been, however, hampered largely by the unfavorable coupling between the quantities σ and κ as well as S and σ in bulk materials. Critically, the electrical conductivity and the electronic part of the thermal conductivity are coupled by the Wiedemann-Franz law,²⁰ while the Seebeck coefficient depends on carrier concentration and is, hence, inversely proportional to the electrical conductivity.

To overcome these tradeoffs, exploitation of quantum confinement effects in hetero- or nano-engineered semiconductors has been suggested to facilitate independent control of S , σ and κ ,²¹ as most convincingly demonstrated in superlattice (SL)-type heterostructures of various different semiconductors, e.g. Bi₂Te₃/Sb₂Te₃ [Ref. 22], Si/Ge [Ref. 23], and III-V materials [Ref. 24]. For group-III nitride thermoelectrics, the role of SL heterostructures has received only very little attention so far. In this respect, Koh et al. reported on cross-plane thermal conductivity of short-period AlN-GaN SLs, revealing details on scattering of phonons in MBE-grown superlattices with abrupt interfaces.²⁵ Furthermore, most recently polarization-engineered wide band-gap GaN-(Al,Ga)N SLs have been introduced by Szein et al. to enable substantially increased electrical conductivity via the formation of high-mobility two-dimensional electron gases (2DEG), while keeping thermal conductivities low.²⁶

In this work, we demonstrate enhanced thermoelectric properties in In-rich InN/InGaN SLs, providing an alternative nitride thermoelectric material. The selection of this lower-band gap class of nitrides is motivated mainly by three distinct factors: (i) InN-based materials (InN and In-rich InGaN) offer very high electron mobility and electrical conductivity ($\sigma > 10^2 \Omega^{-1}\text{cm}^{-1}$),^{27–29} along with one of the highest peak electron velocities ($> 10^8$ cm/s) of any known semiconductor. (ii) Recently, we have demonstrated that InN can exhibit relatively high Seebeck coefficients, both for n-type and p-type materials (up to several hundreds of $\mu\text{V/K}$).^{30,31} (iii) Moreover, the cation/anion mass ratio in InN and In-rich InGaN is the highest in all group-III nitrides, yielding the lowest intrinsic bulk thermal conductivity as well as wide phonon band gaps and narrow acoustic phonon bands.¹⁰

II. EXPERIMENTS

Unintentionally n-type doped InN/InGaN SLs and, for comparison, also In-rich InGaN films were grown by plasma-assisted molecular beam epitaxy (PA-MBE), using conventional effusion cells for group-III elements (Ga,In) and an rf-plasma source for the supply of active nitrogen (N). As substrates we used $\sim 3.5\text{-}\mu\text{m}$ -thick semi-insulating, i.e., iron (Fe)-doped GaN templates on c-plane sapphire. Due to the semi-insulating nature, the influence of the substrate on the thermoelectric properties of the as-grown thin film heterostructures is negligible.^{16,26,31} The (0001)-oriented, metal-polar films and SLs were grown on $10 \times 10 \text{ mm}^2$ substrate pieces under slightly In-rich conditions, using a N-limited equivalent growth rate of $\Phi_{\text{N}} = 6.4 \text{ nm/min}$. For the In-rich InGaN films a series of $\sim 1.1 \text{ }\mu\text{m}$ -thick films were grown with different alloy compositions (nominal values of $0 < x(\text{Ga}) < 0.2$), employing variable Ga-fluxes (equivalent growth rate of $\Phi_{\text{Ga}} = 0.5 - 1.3 \text{ nm/min}$), a fixed In-flux of $\Phi_{\text{In}} = 6.0 \text{ nm/min}$ and growth temperature T^{TC} of $530\text{--}550 \text{ }^\circ\text{C}$ as measured by a thermocouple (TC) attached to the backside of the substrate.³² The respective film structure is schematically depicted in Fig. 1(a). For the InN/InGaN SLs, we have investigated the effect of SL period by varying the InGaN barrier thickness ($d_b = 3 - 40 \text{ nm}$) for a fixed InN quantum well (QW) thickness ($d_{\text{QW}} = 3 \text{ nm}$). For this series, the InGaN alloy composition was fixed to $x(\text{Ga}) = 0.1$, in order to provide a low enough lattice mismatch to the InN wells and thereby preventing enhanced plastic strain relaxation.³³ In total, five SL heterostructures were grown under optimized growth conditions at low T^{TC} of $450 \text{ }^\circ\text{C}$, to avoid inter-diffusion and intermixing between InGaN barriers and InN QWs and to obtain relatively smooth surfaces as confirmed by atomic force microscopy.³² The total film thickness of the InN/InGaN SL heterostructures is equivalent to that of the In-rich InGaN films, i.e., $\sim 1.1 \text{ }\mu\text{m}$.

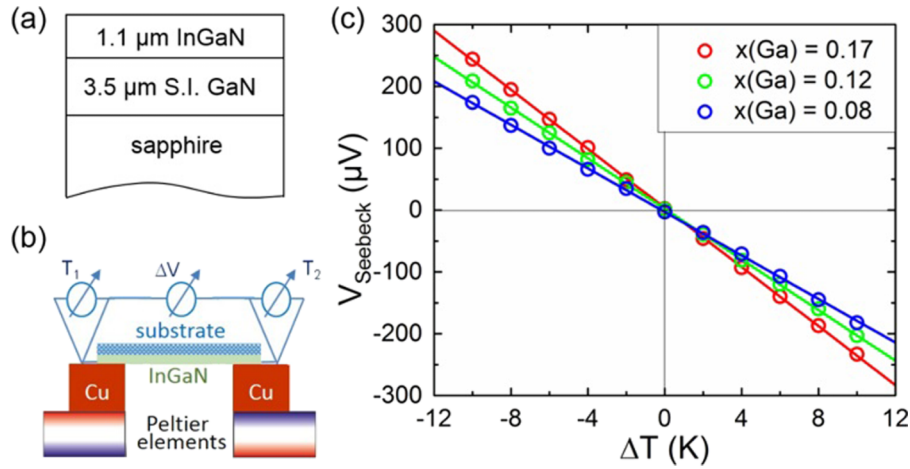


FIG. 1. (a) Schematic illustration of the layer structure for (0001)-oriented In-rich InGaN films deposited on semi-insulating (S.I.) GaN template on c-plane sapphire. (b) Lateral temperature gradient configuration for measurement of in-plane Seebeck coefficient after Ref. 5. (c) Room-temperature Seebeck coefficient measurement for 1.1 μm -thick In-rich InGaN thin films with different Ga-content $x(\text{Ga})$.

After growth, all samples exhibited metallic In droplets on their surface which were removed in buffered hydrochloric acid (HCl). The alloy composition was measured using high-resolution X-ray diffraction (HRXRD) ω -2 θ scans along the (0002) direction and applying Vegard's law, while the InGaN barrier and InN QW thicknesses were determined from HRXRD interference fringes. The electrical conductivity, carrier concentration (n_e) and mobility (μ) of the unintentionally n-type doped films were obtained by in-plane Hall effect measurements via the van der Pauw method using soldered In contacts. In-plane Seebeck coefficients were extracted from measurements performed in the lateral temperature gradient geometry using a home-built setup⁵ as depicted in Fig. 1(b). Here, the voltage drop was measured which develops across the sample due to a temperature gradient realized by two temperature-controlled copper blocks at each side of the sample (see Fig. 1(c)). Finally, the cross-plane thermal conductivity (κ) was measured by a pump-probe technique called time-domain thermoreflectance (TDTR).³⁴ We employed a two-tint approach to reject the diffusely scattered pump laser from being measured by our system.³⁵ In TDTR measurements, we coat the as-grown samples with ~ 100 -nm-thick Al films as the transducer. We then apply a pump beam with a modulation frequency of 0.5 MHz and 1 MHz to periodically heat the samples. We use a probe beam to monitor the temperature response at sample surface via the change of reflectance of the Al transducer with temperature (i.e., thermoreflectance). Here, we used a laser power of ~ 30 mW and laser $1/e^2$ radii of 11 μm , with temperature rises of ~ 6 K. We design the experiments such that the heat transfer is primarily one-dimensional in the cross-plane direction. We derived the cross-plane thermal conductivity by comparing our measurements to calculations of the thermal model in Refs. 36 and 37. All measurements of σ , S , and κ were performed at room-temperature.

III. RESULTS AND DISCUSSION

A. Thermoelectric properties of In-rich InGaN alloys

First, we investigate the thermoelectric properties of the In-rich InGaN ternary alloys. Fig. 1(c) shows the Seebeck voltage versus applied temperature gradient ΔT as measured for three In-rich InGaN films with different Ga-content $x(\text{Ga})$. The slope of ΔV versus ΔT is linear and gives the sign and magnitude of the resulting Seebeck coefficient. The final Seebeck coefficient is further corrected by the Seebeck coefficient of the connecting electrical wires and copper blocks ($S_c = 4.1 \mu\text{V/K}$). As a result, the final Seebeck coefficient for the three InGaN films is negative, indicative of the unintentional n-type conductivity, and increases slightly in magnitude with increasing Ga-content, i.e., $S = -13 \mu\text{V/K}$ [$x(\text{Ga}) = 0.08$], $S = -15.5 \mu\text{V/K}$ [$x(\text{Ga}) = 0.12$], and $S = -20 \mu\text{V/K}$ [$x(\text{Ga})$

TABLE I. Average electron mobility (μ), electron concentration (n_e), corresponding electrical conductivity (σ) and Seebeck coefficient (S) for InGaN films with different Ga-content $x(\text{Ga})$ as measured at 300 K.

InGaN film $x(\text{Ga})$	mobility μ (cm^2/Vs)	electron density n_e (cm^{-3})	conductivity σ (Ωcm) $^{-1}$	Seebeck coeff. ($\mu\text{V/K}$)
0	831	1.6×10^{19}	2.1×10^3	-34
0.08	304	4.4×10^{19}	2.2×10^3	-13
0.12	338	5.1×10^{19}	2.8×10^3	-15
0.17	321	5.6×10^{19}	2.9×10^3	-20

= 0.17]. Since the In-rich InGaN films are strongly degenerate with high electron concentrations of $n_e \sim 4.4\text{--}5.6 \times 10^{19} \text{ cm}^{-3}$ (see Table I), the Seebeck coefficient is related to the generic expression $S = \frac{8\pi^2 k_B^2}{3eh^2} m^* \left(\frac{\pi}{3n_e} \right)^{\frac{2}{3}} T$, as derived from the relaxation time approximation of Boltzmann's transport equation in the degenerate semiconductor limit.³⁸ This analytic expression may not account for the precise non-parabolic band dispersion of In-rich InGaN,^{30,31} yielding slightly underestimated values for the calculated Seebeck coefficient as compared to the as-measured values. For instance, for the InN reference the calculated S is $-22 \mu\text{V/K}$, while the measured value amounts to $-34 \mu\text{V/K}$ (see Table I). Nevertheless, the analytic expression still approximates the direct dependence of S on electron effective mass (m^*) and the inverse relationship on carrier concentration (n_e), with e being the electron charge, h the Planck constant, k_B the Boltzmann constant, and T the absolute temperature, respectively. Hence, the experimentally observed increase of the Seebeck coefficient with rising Ga-content seems to reflect the increase of the electron effective mass as the Ga-content of the InGaN films becomes larger. This is supported by the fact that n_e only varies slightly in the InGaN films (see Table I), whereby any slight increase in n_e would actually induce a reduction in the magnitude of the Seebeck coefficient. In addition, temperature-dependent Seebeck coefficient measurements performed between 300 K and 700 K (not shown) illustrate a fully linear increase in the magnitude of the Seebeck coefficient with temperature, confirming the validity of the degenerate approximation. Despite the observed trends in Seebeck coefficient with variable Ga-content, the obtained values are overall limited by the high electron concentrations in the In-rich InGaN films.

Based on the Hall-measured electron concentrations and mobilities we further determined the electrical conductivity values, as given in Table I and Fig. 2(a). We obtain very high values of $\sigma \sim 2\text{--}3 \times 10^3 (\Omega\text{cm})^{-1}$ with a tendency towards slightly higher values with increasing Ga-content $x(\text{Ga})$. These values are typically about one to two orders of magnitude higher as compared to other nitride alloys studied for thermoelectrics, e.g. AlInN [Ref. 15] or high Ga-content InGaN [Refs. 11–13] films grown by other methods. The high conductivity values obtained in this work are mainly due to the considerably higher mobilities despite of the high unintentional background

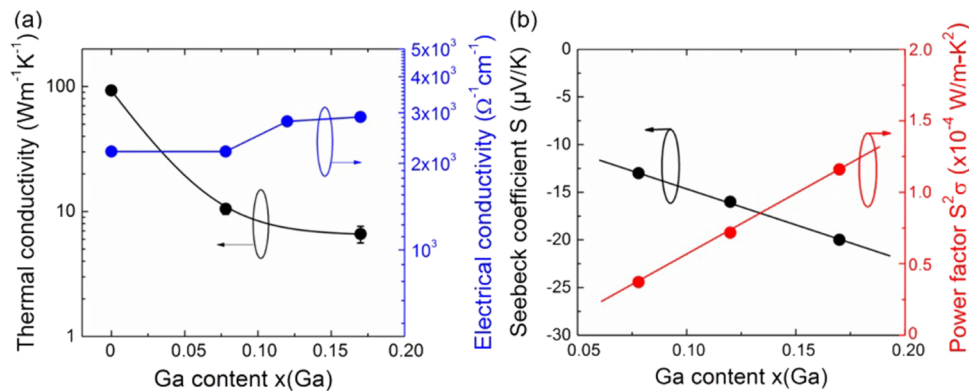


FIG. 2. (a) Thermal conductivity (black data) and electrical conductivity (blue data) as a function of Ga-content $x(\text{Ga})$ for the different In-rich InGaN films; (b) Seebeck coefficient (S) (black data) and thermoelectric power factor ($S^2\sigma$) (red data) for the different InGaN films with comparable carrier density. All data is obtained at room-temperature.

electron concentrations. Typically, in In-rich InGaN films the relatively high threading dislocation (TD) densities ($>10^9 \text{ cm}^{-2}$) act as mobility-limiting scattering centers in low-carrier density In-rich InGaN films ($n_e \sim 10^{17}\text{--}10^{18} \text{ cm}^{-3}$) [Ref. 39]. In contrast, in high-carrier density films ($n_e > \sim 5 \times 10^{18} \text{ cm}^{-3}$) the increased electron concentration strongly screens the charged dislocations.^{31,40} Given the fact that the TD density increases with increasing Ga-content in our In-rich InGaN films,³² we can conclude that the electron mobility is hence mainly governed by residual impurity and alloy scattering. Indeed, alloy scattering might be considered as a prominent scattering mechanism in In-rich InGaN films, since they are prone to alloy compositional fluctuations³² and formation of metallic In precipitates⁴¹ particularly when grown under In-rich conditions.

In contrast to the relatively unchanged electrical conductivity, the thermal conductivity is drastically influenced by increased alloying. As shown in Fig. 2(a), the cross-plane thermal conductivity is reduced by more than a factor of 10 from $\kappa = 95 \text{ W/m-K}$ for InN to $\kappa = 6.5 \text{ W/m-K}$ for InGaN with $x(\text{Ga}) = 0.17$. Comparable reductions in the thermal conductivity are observed in other nitride alloys.^{3,11,13–16,42} As a result of alloying, high-energy phonons that contribute to most of heat transport in InN at higher temperature are strongly scattered by Rayleigh scattering, due to disorder in mass and strength of bonds of In and Ga atoms.^{7,42} As known from other alloy systems, alloying is thereby an effective approach to reduce the thermal conductivity of crystals. We note that since κ was measured in cross-plane direction, the values presented here are the lower limits for the thermal conductivity in the in-plane direction. The difference between the values in the in-plane and cross-plane directions should be relatively small, since the film is sufficiently thick and that it is common to approximate κ in thin-film thermoelectrics from the values in the cross-plane direction.^{7,11,13,19} Furthermore, the observation of significantly reduced κ by alloying without deterioration of electrical properties is one of the key benefits of alloyed materials for thermoelectrics.^{7,17,22} The thermoelectric power factor ($S^2\sigma$), which combines electrical conductivity and Seebeck coefficient, is further plotted in Fig. 2(b). We find a gradual rise in the power factor with increasing Ga-content, yielding $>10^{-4} \text{ W/m-K}^2$ for the InGaN film with $x(\text{Ga}) = 0.17$ – i.e., values of the same order of magnitude as e.g. InAlN [Refs. 15 and 16] and Ga-rich InGaN [Ref. 13]. The power factor together with the thermal conductivity yield a room-temperature ZT value of 0.006 for the InGaN film with $x(\text{Ga}) = 0.17$, which is slightly lower than found in e.g. optimized Ga-rich InGaN films [Ref. 13]. We note that in our work the electron concentration and the respective trade-off between Seebeck coefficient and electrical conductivity are not yet optimized for the high In-content InGaN films. Nevertheless, highly degenerate carrier densities in the order of $\sim 5 \times 10^{18}\text{--}10^{20} \text{ cm}^{-3}$ are considered most suitable for highest power factors in nitride alloys^{13,15,16} as well as other semiconductor systems.^{19,38}

B. Thermoelectric properties of InN/InGaN superlattices

To investigate whether the thermoelectric properties can be enhanced beyond the alloy limit, we turn our attention now to short-period In-rich InN/InGaN SLs. Here, intentional electron quantum confinement effects and additional boundary phonon scattering via well-controlled heterointerfaces are expected to enable more independent control of σ , S and κ .^{22–24} Figs. 3(a) and 3(b) illustrate the representative layer structure and a 7-period wide section of the electronic band profile of a typical short-period InN/InGaN thin film SL, as calculated based on self-consistent solutions of Schrödinger-Poisson equations using the nextnano³ simulator.⁴³ The simulated layer structure used here takes into account the spontaneous and piezoelectric fields and consists of 3-nm-thin InN QWs and 10-nm-wide InGaN barriers [$x(\text{Ga}) = 0.1$] with a total electron concentration of $n_e = 1 \times 10^{19} \text{ cm}^{-3}$. Also indicated is the confined ground state energy for the electron wavefunction in the conduction band (CB), which has been further simulated as a function of barrier thickness d_b under fixed well thickness ($d_{\text{QW}} = 3 \text{ nm}$) (not shown). From the simulations we note that the squared electron wavefunction penetrates into the InGaN barriers for $d_b/d_{\text{QW}} > 3$, while much stronger confinement is achieved for $d_b/d_{\text{QW}} < 2$, i.e., very short-period SLs. This is important from a thermoelectric perspective, since confined electrons in a high-mobility 2DEG at the InN/InGaN heterointerfaces may allow for enhanced electron mobility and electrical conductivity,²⁶ as further shown below.

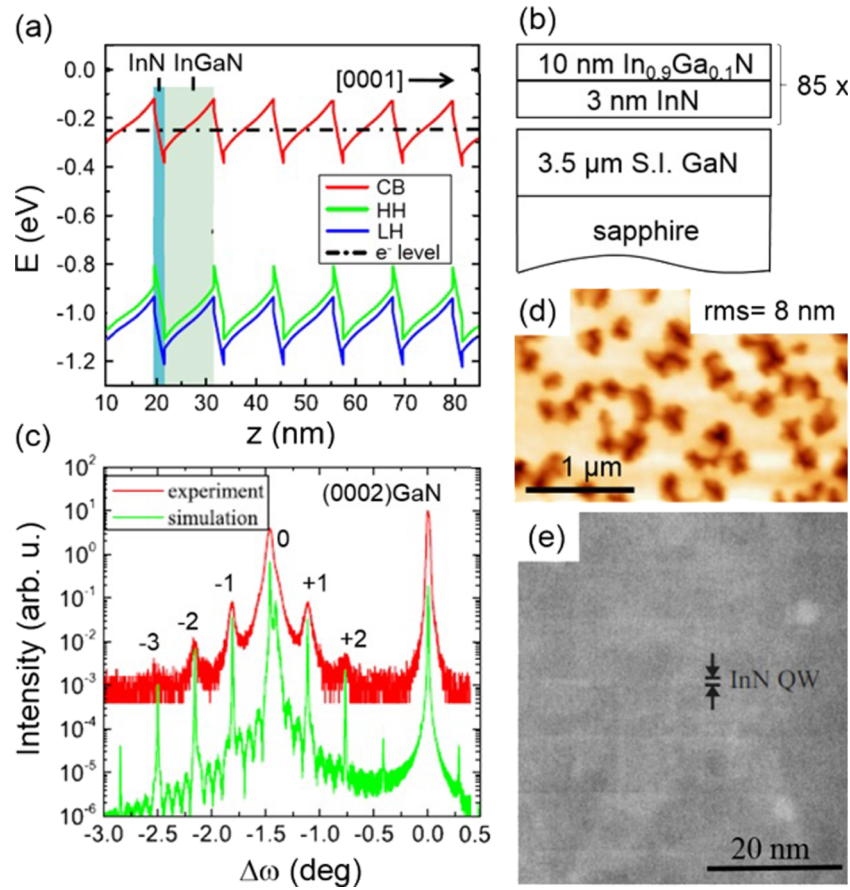


FIG. 3. (a) Electronic band profile for a section of a short-period InN/InGaN superlattice (SL) with a layer structure as depicted in (b); band structure calculations are performed for a background electron density of $1 \times 10^{19} \text{ cm}^{-3}$ using nextnano.³ (c) Measured and simulated (0002) HRXRD ω -2 θ spectra of an 85-period 3-nm-InN/10-nm-InGaN [$x(\text{Ga})=0.1$] SL. (d) $2 \times 3 \mu\text{m}^2$ AFM surface morphology of the same SL structure with rms roughness of ~ 8 nm; height scale of the image is 50 nm. (e) Corresponding cross-sectional TEM micrograph ($[11\bar{2}0]$ zone axis) taken midway through the layer thickness.

Figures 3(c)-3(e) present the structural and morphological properties of an exemplary as-grown short-period InN/InGaN SL according to the layer structure of Fig. 3(b). The (0002) HRXRD ω -2 θ scan of Fig. 3(c) exhibits the peak reflections of the GaN template and the InN/InGaN SL structure. The interference fringes from the SL structure indicate clear satellite peaks up to third order, which are well lined up with the simulated data using the nominal parameters for d_b (10 nm), d_{QW} (3 nm), and $x(\text{Ga}) = 0.1$. The large number of observed satellite peaks demonstrates good periodicity and sharp interfaces across the 85-period, $\sim 1.1 \mu\text{m}$ -thick SL structure. This is further confirmed by a cross-sectional transmission electron microscopy (TEM) image recorded along the $[11\bar{2}0]$ zone axis of the same sample (Fig. 3(e)). The periodic bright contrast stripes propagating in the horizontal direction illustrate the ~ 3 -nm-thin InN QWs. The corresponding surface morphology, as measured by atomic force microscopy (AFM) in Fig. 3(d), reveals an overall flat surface obscured by a high density of deep surface pits with an average density of $\sim 1 \times 10^9 \text{ cm}^{-2}$. We associate these pits to open core screw-component TDs, according to their very similar density observed in InN-based heteroepitaxial films on GaN.⁴⁴ Due to the deep surface pits the root-mean-square (rms) roughness of the as-grown SL structure amounts to ~ 8 nm over the given AFM scan area.

Similar to the previous measurements performed for In-rich InGaN alloys, the in-plane Seebeck coefficients, electrical conductivity, electron concentration and mobility, as well as thermoelectric power factor are evaluated in Fig. 4 for the In-rich InN/InGaN SLs. In particular, we investigate a series of short-period SL with variable barrier thickness d_b (3 – 40 nm) at fixed InN QW

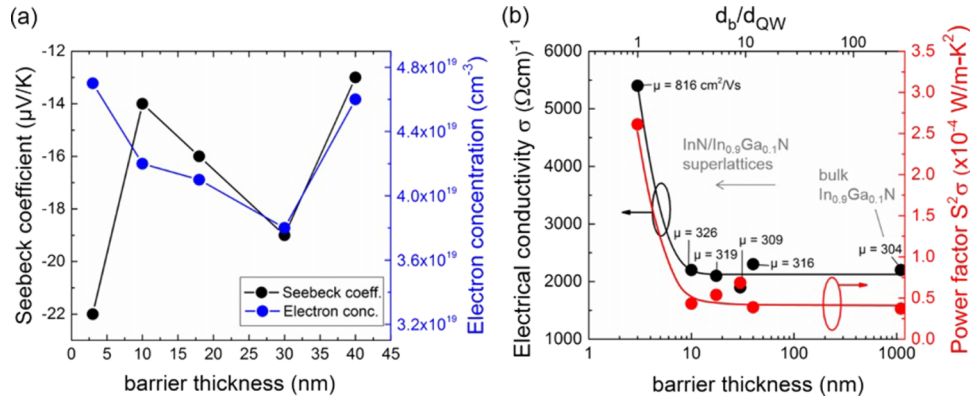


FIG. 4. (a) Seebeck coefficient (black data) and electron concentration (blue data) for 1.1- μm -thick InN/InGaN superlattice films with fixed InN QW thickness ($d_{\text{QW}} = 3$ nm) but variable InGaN barrier thickness ($d_b = 3$ –40 nm). (b) Corresponding electrical conductivity (black data) and thermoelectric power factor (red data) obtained for the same sample series. Respective electron mobility data is also given for each datapoint; for comparison also an InGaN reference sample (equivalent barrier thickness of 1100 nm and identical $x(\text{Ga}) = 0.1$) is shown.

thickness of 3 nm. Interestingly, the data shows that, while large barrier thickness ($d_b > 10$ nm) has only a negligible effect on enhancement of thermoelectric properties, small barrier thickness (e.g. $d_b = 3$ nm) yields a significant enhancement on the power factor due to the much stronger charge carrier confinement. This major enhancement is mainly attributed to the strongly increased electrical conductivity due to substantially higher electron mobilities in very short-period SLs, as compared to wider-period SL and ternary In-rich InGaN alloy reference films. Although the background electron concentration is more or less constant throughout this series ($n_e \sim 3.8 - 4.7 \times 10^{19} \text{ cm}^{-3}$), the mobility increases up to $816 \text{ cm}^2/\text{Vs}$ for the very short-period SL structure. This is roughly a factor of 3 higher as compared to pure ternary InGaN alloys.

Such an enhanced mobility translates into an electrical conductivity as high as $\sigma = 5400 (\Omega\text{cm})^{-1}$, a conductivity which is nearly five times larger than previously realized in intentionally doped GaN-(Al,Ga)N SL thermoelectric structures.²⁶ In agreement with the simulations, the high mobility is expected as a result of the much stronger electron confinement in the very short-period InN/InGaN SL structure with $d_b/d_{\text{QW}} = 1$. Essentially, as for this case the electron wave-function confined in the InN QW penetrates only very little into the adjacent InGaN barrier, the electrons are much less exposed to alloy scattering and charged dislocation scattering due to effective screening by the locally higher electron densities.

As seen in Fig. 4(a), the measured Seebeck coefficient is also slightly influenced by the electron confinement properties. For wide-period SLs ($d_b > 10$ nm), which electronically resemble bulk-like ternary InGaN alloys due to poor confinement, the Seebeck coefficient scales inversely with the electron concentration as typically expected by the strong coupling between S and n_e in degenerate semiconductors.^{30,31,38} In contrast, for the very short-period SL structure ($d_b = 3$ nm), the linkage between S and n_e appears to be slightly decoupled and the Seebeck coefficient increases up to $S = 22 \mu\text{V/K}$ despite the overall higher electron concentration. This suggests that the stronger two-dimensional (2D) confinement shifts the optimum Fermi energy to a lower value, which was confirmed by simulations of the Fermi level position relative to the conduction band edge and electron ground state of the InN QW, respectively. The observed effect, therefore, likely illustrates the generally expected enhancement of the Seebeck coefficient by confinement effects in 2D-QWs of short-period SL structures as suggested by Hicks and Dresselhaus.²¹ Further theoretical modelling and electronic transport measurements along other directions, such as the cross-plane, are however needed to verify these effects fully quantitatively. Combining the measured Seebeck coefficients and electrical conductivities for the different SL samples, the power factors are calculated, yielding values up to $> 2.5 \times 10^{-4} \text{ W/m-K}^2$ for the very short-period SL. For the given Ga-content of $x(\text{Ga}) = 0.1$, this is a more than 5-fold increase in power factor as compared to the ternary InGaN alloy reference, demonstrating the viability of short-period SL heterostructures.

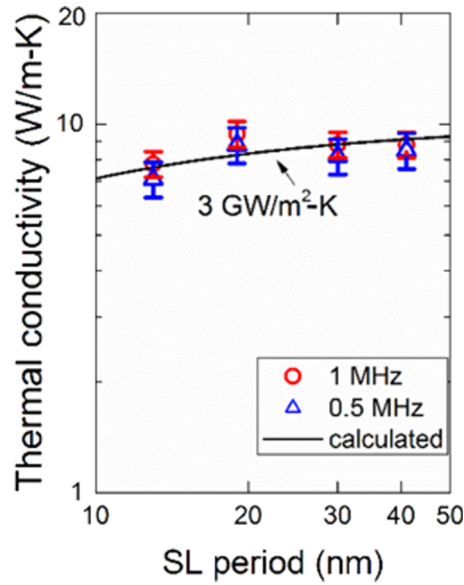


FIG. 5. Cross-plane thermal conductivity of the short-period InN/InGaN SLs as a function of SL period, measured at two different modulation frequencies. The experimental data is further calculated based on a simple model as described in the text, with the thermal conductance G as a fitting parameter. Best fits are obtained for $G = 3 \text{ GW/m}^2\text{-K}$.

Finally, the cross-plane thermal conductivity (κ) for the InN/InGaN SL structures are presented in Fig. 5 as a function of SL period. Measurements using modulation frequencies of 0.5 and 1 MHz, respectively, are plotted. The deviation between the two obtained datasets is nearly negligible, with uncertainties of 11% (at 0.5 MHz) and 8% (at 1 MHz), respectively. Overall, the thermal conductivity is found to slightly decrease with decreasing SL period, i.e., from $\kappa = 8.6 \text{ W/m-K}$ for $d_b = 40 \text{ nm}$ to $\kappa = 7.1 \text{ W/m-K}$ for $d_b = 10 \text{ nm}$ at 0.5 MHz. Our measurements are compared with calculations of a simple model that assumes that the thermal resistance of individual layers and interfaces adds in series; $\frac{d_{QW}+d_b}{\kappa} = \frac{d_{QW}}{\kappa(\text{InN})} + \frac{d_b}{\kappa(\text{InGaN})} + \frac{2}{G}$ [Ref. 25], where d_{QW} and d_b are the thicknesses of InN QW and InGaN barrier, κ is the as-measured thermal conductivity of the SL, $\kappa(\text{InN}) = 95 \text{ W/m-K}$ and $\kappa(\text{InGaN}) = 10 \text{ W/m-K}$ are the bulk thermal conductivities as extracted in Fig. 2(a), and G represents the thermal conductance used as a free fitting parameter.

Best fits to the data yield a very high interfacial thermal conductance of $G = 3 \text{ GW/m}^2\text{-K}$ at the InN/InGaN SL interfaces, i.e., a value which is commonly observed in short-period SL even in other semiconductors such as e.g. AlN-GaN SLs [Ref. 25] or GaAs/AlGaAs SLs [Ref. 45]. This high value of G is probably due to the fact that low-energy phonons are not strongly scattered by the interfaces, as explained in Ref. 25. By further comparing the obtained cross-plane thermal conductivity data of the InN/InGaN SLs with those of ternary InGaN bulk alloy reference samples ($\kappa(\text{InGaN}) \sim 10 \text{ W/m-K}$ for $x(\text{Ga}) = 0.1$), it is worth noting that the thermal conductivity of the SLs is only slightly smaller. This is consistent with previous studies on AlN/GaN SLs, in which the thermal conductivity of short-period SLs approaches the alloy limit.²⁵

IV. CONCLUSIONS

In conclusion, we have explored the thermoelectric properties of MBE-grown short-period InN/InGaN superlattices (SL) in comparison with ternary In-rich InGaN alloy films. By investigating the effect of SL period, i.e., variable InGaN barrier thickness under fixed InN QW width, we identify very short-period SL structures with good charge carrier confinement properties as promising structures with remarkable increases in electrical conductivity and thermoelectric power factor over ternary InGaN alloys. In addition, very short-period SLs also appear to decouple Seebeck coefficient from electron concentration, and further give thermal conductivity values approaching the

alloy limit. These results demonstrate the potentials of In-rich group-III nitride-based superlattice heterostructures as an interesting class of thermoelectric materials.

The authors thank Evans Analytical Group for TEM measurements. Financial support by TUM.solar in the framework of the Bavarian Collaborative Research Project “Solar technologies go Hybrid” (SolTec) is gratefully acknowledged. Furthermore, we thank the DFG excellence program Nanosystems Initiative Munich (NIM) for facilities support. This work is partially supported by the Singapore Ministry of Education Academic Research Fund Tier 1 Start-up Grant.

- ¹ S. Pimpitkar, J. S. Speck, S. P. DenBaars, and S. Nakamura, *Nature Photon.* **3**, 180 (2009).
- ² U. K. Mishra, L. Shen, T. E. Kazior, and Y.-F. Wu, *Proc. IEEE* **96**, 287 (2008).
- ³ S. Yamaguchi, Y. Iwamura, and A. Yamamoto, *Appl. Phys. Lett.* **82**, 2065 (2003).
- ⁴ S. Yamaguchi, R. Izaki, N. Kaiwa, S. Sugimura, and A. Yamamoto, *Appl. Phys. Lett.* **84**, 5344 (2004).
- ⁵ M. S. Brandt, P. Herbst, H. Angerer, O. Ambacher, and M. Stutzmann, *Phys. Rev. B* **58**, 7786 (1998).
- ⁶ A. Szein, H. Ohta, J. Sonoda, A. Ramu, J. E. Bowers, S. P. DenBaars, and S. Nakamura, *Appl. Phys. Exp.* **2**, 111003 (2009).
- ⁷ W. L. Liu and A. A. Balandin, *J. Appl. Phys.* **97**, 073710 (2005).
- ⁸ S. Yamaguchi, R. Izaki, N. Kaiwa, and A. Yamamoto, *Appl. Phys. Lett.* **86**, 252102 (2005).
- ⁹ R. Izaki, N. Kaiwa, M. Hoshino, T. Yaginuma, S. Yamaguchi, and A. Yamamoto, *Appl. Phys. Lett.* **87**, 243508 (2005).
- ¹⁰ A. X. Levander, T. Tong, K. M. Yu, J. Suh, D. Fu, R. Zhang, H. Lu, W. J. Schaff, O. Dubon, W. Walukiewicz, D. G. Cahill, and J. Wu, *Appl. Phys. Lett.* **98**, 012108 (2011).
- ¹¹ B. N. Pantha, R. Dahal, J. Li, J. Y. Lin, H. X. Jiang, and G. Pomrenke, *Appl. Phys. Lett.* **92**, 042112 (2008).
- ¹² B. N. Pantha, R. Dahal, J. Li, J. Y. Lin, H. X. Jiang, and G. Pomrenke, *J. Electron Mater.* **38**, 1132 (2009).
- ¹³ A. Szein, H. Ohta, J. E. Bowers, S. P. DenBaars, and S. Nakamura, *J. Appl. Phys.* **110**, 123709 (2011).
- ¹⁴ H. Tong, J. Zhang, G. Liu, J. A. Herbsommer, G. S. Huang, and N. Tansu, *Appl. Phys. Lett.* **97**, 112105 (2010).
- ¹⁵ J. Zhang, H. Tong, G. Liu, J. A. Herbsommer, G. S. Huang, and N. Tansu, *J. Appl. Phys.* **109**, 053706 (2011).
- ¹⁶ A. Szein, J. E. Bowers, S. P. DenBaars, and S. Nakamura, *J. Appl. Phys.* **112**, 083716 (2012).
- ¹⁷ J. Piprek, *Semiconductor Optoelectronic Devices* (Academic, San Diego, 2003).
- ¹⁸ W. Nakwaski, *J. Appl. Phys.* **64**, 159 (1988).
- ¹⁹ J.-H. Bahk, Z. Bian, M. Zebarjadi, J. M. O. Zide, H. Lu, D. Xu, J. P. Feser, G. Zeng, A. Majumdar, A. C. Gossard, A. Shakouri, and J. E. Bowers, *Phys. Rev. B* **81**, 235209 (2010).
- ²⁰ A. Bejan and A. D. Allan, *Heat Transfer Handbook* (Wiley, New York, 2003).
- ²¹ L. D. Hicks and M. S. Dresselhaus, *Phys. Rev. B* **47**, 12727 (1993).
- ²² R. Venkatasubramanian, E. Siivola, T. Colpitts, and B. O’Quinn, *Nature* **413**, 597 (2001).
- ²³ T. Koga, S. B. Cronin, M. S. Dresselhaus, J. L. Liu, and K. L. Wang, *Appl. Phys. Lett.* **77**, 1490 (2000).
- ²⁴ G. Zeng, J. M. O. Zide, W. Kim, J. E. Bowers, A. C. Gossard, Z. Bian, Y. Zhang, A. Shakouri, S. L. Singer, and A. Majumdar, *J. Appl. Phys.* **101**, 034502 (2007).
- ²⁵ Y. K. Koh, Y. Cao, D. G. Cahill, and D. Jena, *Adv. Funct. Mater.* **19**, 610 (2009).
- ²⁶ A. Szein, J. E. Bowers, S. P. DenBaars, and S. Nakamura, *Appl. Phys. Lett.* **104**, 042106 (2014).
- ²⁷ G. Koblmüller, C. S. Gallinat, S. Bernardis, J. S. Speck, G. D. Chern, E. D. Readinger, H. Shen, and M. Wraback, *Appl. Phys. Lett.* **89**, 071902 (2006).
- ²⁸ B. Loitsch, F. Schuster, M. Stutzmann, and G. Koblmüller, *Appl. Phys. Lett.* **102**, 051916 (2013).
- ²⁹ M. Himmerlich, A. Knübel, R. Aidam, L. Kirste, A. Eisenhardt, S. Krischok, J. Pezoldt, P. Schley, R. Goldhahn, and G. Koblmüller, *J. Appl. Phys.* **113**, 033501 (2013).
- ³⁰ N. Miller, J. W. Ager III, H. M. Smith III, M. A. Mayer, K. M. Yu, E. E. Haller, W. Walukiewicz, W. J. Schaff, C. S. Gallinat, G. Koblmüller, and J. S. Speck, *J. Appl. Phys.* **107**, 113712 (2010).
- ³¹ N. Miller, E. E. Haller, G. Koblmüller, C. S. Gallinat, J. S. Speck, W. J. Schaff, M. E. Hawkrige, K. M. Yu, and J. W. Ager III, *Phys. Rev. B* **84**, 075315 (2011).
- ³² J. Ju, B. Loitsch, T. Stettner, F. Schuster, M. Stutzmann, and G. Koblmüller, *J. Appl. Phys.* **116**, 053501 (2014).
- ³³ G. D. Chern-Metcalf, E. D. Readinger, H. Shen, M. Wraback, G. Koblmüller, C. S. Gallinat, and J. S. Speck, *Phys. Stat. Sol. (c)* **5**, 1846 (2008).
- ³⁴ D. G. Cahill, W. K. Ford, K. E. Goodson, G. D. Mahan, A. Majumdar, H. J. Maris, R. Merlin, and S. R. Phillpot, *J. Appl. Phys.* **93**, 793 (2003).
- ³⁵ K. Kang, Y. K. Koh, C. Chiriac, X. Zheng, and D. G. Cahill, *Rev. Sci. Instrum.* **79**, 114901 (2008).
- ³⁶ D. G. Cahill, *Rev. Sci. Instrum.* **75**, 5119 (2004).
- ³⁷ Y. K. Koh and D. G. Cahill, *Phys. Rev. B* **76**, 075207 (2007).
- ³⁸ G. J. Snyder and E. S. Toberer, *Nature Mater.* **7**, 105 (2008).
- ³⁹ C. S. Gallinat, G. Koblmüller, and J. S. Speck, *Appl. Phys. Lett.* **95**, 022103 (2009).
- ⁴⁰ X. Wang, S. Liu, N. Ma, L. Feng, G. Chen, F. Xu, N. Tang, S. Huang, K. J. Chen, S. Zhou, and B. Shen, *Appl. Phys. Exp.* **5**, 015502 (2012).
- ⁴¹ S. V. Ivanov, T. V. Shubina, T. A. Komissarova, and V. N. Jmerik, *J. Cryst. Growth* **403**, 83 (2014).
- ⁴² V. Rawat, Y. K. Koh, D. G. Cahill, and T. D. Sands, *J. Appl. Phys.* **105**, 024909 (2009).
- ⁴³ S. Birner, T. Zibold, T. Andlauer, T. Kubis, M. Sabathil, A. Trellakis, and P. Vogl, *IEEE Trans. Electron Dev.* **54**, 2137 (2007).
- ⁴⁴ C. S. Gallinat, G. Koblmüller, F. Wu, and J. S. Speck, *J. Appl. Phys.* **107**, 053517 (2010).
- ⁴⁵ W. S. Capinski, H. J. Maris, T. Ruf, M. Cardona, K. Ploog, and D. S. Katzner, *Phys. Rev. B* **59**, 8105 (1999).